

THE CIRCUMGALACTIC MEDIUM OF MASSIVE GALAXIES AT $Z \sim 3$: A TEST FOR STELLAR FEEDBACK, GALACTIC OUTFLOWS, AND COLD STREAMS

SIJING SHEN¹, PIERO MADAU¹, JAVIERA GUEDES², LUCIO MAYER³, J. XAVIER PROCHASKA^{1,4}, & JAMES WADSLEY⁵

Submitted to the Astrophysical Journal

ABSTRACT

We present new results on the kinematics, thermal and ionization state, and spatial distribution of metal-enriched gas in the circumgalactic medium (CGM) of massive galaxies at redshift ~ 3 , using the “Eris” suite of cosmological hydrodynamic “zoom-in” simulations. The reference run adopts a blastwave scheme for supernova feedback that produces large-scale galactic outflows, a star formation recipe based on a high gas density threshold, metal-dependent radiative cooling, and a model for the diffusion of metals and thermal energy. The effect of the local UV radiation field is added in post-processing. The CGM (defined as all gas at $R > 0.2R_{\text{vir}} = 10$ kpc, where R_{vir} is the virial radius) contains multiple phases having a wide range of physical conditions, with more than half of its heavy elements locked in a warm-hot component at $T > 10^5$ K. Synthetic spectra, generated by drawing sightlines through the CGM, produce interstellar absorption line strengths of Ly α , C II, C IV, Si II, and Si IV as a function of galactocentric impact parameter (scaled to the virial radius) that are in broad agreement with those observed at high-redshift by Steidel et al. (2010). The covering factor of absorbing material declines less rapidly with impact parameter for Ly α and C IV compared to C II, Si IV, and Si II, with Ly α remaining strong ($W_{\text{Ly}\alpha} > 300$ mÅ) to $\gtrsim 5R_{\text{vir}} = 250$ kpc. Only about one third of all the gas within R_{vir} is outflowing. The fraction of sightlines within one virial radius that intercept optically thick, $N_{\text{HI}} > 10^{17.2} \text{ cm}^{-2}$ material is 27%, in agreement with recent observations by Rudie et al. (2012). Such optically thick absorption is shown to trace inflowing “cold” streams that penetrate deep inside the virial radius. The streams, enriched to metallicities above 0.01 solar by previous episodes of star formation in the main host and in nearby dwarfs, give origin to strong ($N_{\text{CII}} > 10^{13} \text{ cm}^{-2}$) C II absorption with a covering factor of 22% within R_{vir} and 10% within $2R_{\text{vir}}$. Galactic outflows do not cause any substantial suppression of the cold accretion mode. The central galaxy is surrounded by a large O VI halo, with a typical column density $N_{\text{OVI}} \gtrsim 10^{14} \text{ cm}^{-2}$ and a near unity covering factor maintained all the way out to 150 kpc. This matches the trends recently observed in star-forming galaxies at low redshift by Tumlinson et al. (2011). Our zoom-in simulations of this single system appear then to reproduce quantitatively the complex baryonic processes that determine the exchange of matter, energy, and metals between galaxies and their surroundings.

Subject headings: galaxies: evolution – galaxies: high-redshift – intergalactic medium – method: numerical

1. INTRODUCTION

Studies of the ionization, chemical, thermodynamic, and kinematic state of gaseous material in the circumgalactic medium (CGM) hold clues to understanding the exchange of mass, metals, and energy between galaxies and their surroundings. It is the poorly understood flows of gas into galaxies, and from them back into their environments, that determine the response of baryons to dark matter potential wells, regulate star formation, and enrich the intergalactic medium (IGM). Observations clearly show that galactic-scale metal-rich outflows with velocities of several hundred km s^{-1} are ubiquitous in massive star-forming galaxies at high redshift (e.g., Pettini et al. 2001; Shapley et al. 2003; Veilleux et al.

2005; Weiner et al. 2009). Far-UV spectra of close angular pairs of $z \sim 2$ -3 “Lyman Break Galaxies” (LBGs) have recently provided a detailed map of such metal-enriched gas as a function of galactocentric distance (Steidel et al. 2010), and a benchmark for simulations of the galaxy-IGM ecosystem. The observed line strengths of several ionic species convey information about the physical conditions, covering fraction, and velocity spread of the absorbing multi-phase CGM on 100 kpc scales (Steidel et al. 2010). These, together with the increasing amount of data that has been accumulated recently on the galaxy environs at high and low redshifts (e.g. Prochaska & Hennawi 2009; Crighton et al. 2011; Prochaska et al. 2011; Tumlinson et al. 2011; Rudie et al. 2012), must be reproduced by hydrodynamical simulations of galaxy formation that aim at following the transport of heavy elements from their production sites into the IGM (e.g. Oppenheimer & Davé 2008; Wiersma et al. 2009; Shen et al. 2010; Cen & Chisari 2011).

Recent theoretical work has found that the majority of baryons accreted by galaxies below a certain critical mass flow in “cold” rather than being shocked

¹ Department of Astronomy and Astrophysics, University of California, 1156 High Street, Santa Cruz, CA 95064.

² Institute for Astronomy, ETH Zurich, Wolfgang-Pauli-Strasse 27, 8093 Zurich, Switzerland.

³ Institute of Theoretical Physics, University of Zurich, Winterthurerstrasse 190, CH-9057 Zurich, Switzerland.

⁴ UCO/Lick Observatory, University of California, 1156 High Street, Santa Cruz, CA 95064.

⁵ Department of Physics & Astronomy, McMaster University, Hamilton, ON L8S 4M1, Canada.

to the virial temperature (e.g. Birnboim & Dekel 2003; Kereš et al. 2005; Dekel & Birnboim 2006; Ocvirk, Pichon, & Teyssier 2008; Dekel et al. 2009; Kereš et al. 2009). This cold accretion mode occurs mainly along dense streams that deliver fresh fuel for star formation to the disk (e.g. Brooks et al. 2009). Even when a shock is present, cold gas accretion can occur along filaments that penetrate deep inside the hot halo (e.g. Dekel & Birnboim 2006; Dekel et al. 2009; Agertz, Teyssier, & Moore 2009). Signatures of such streams may include Ly α blobs (Goerdt et al. 2010), Lyman Limit Systems (Fumagalli et al. 2011), or Mg II absorbers (Kacprzak et al. 2012). Previous numerical studies on cold flows and the cycle of baryons in and out of galaxies have either focused on a statistical description of how galaxies get their gas and sacrificed numerical resolution on individual galaxy scales (e.g. Kereš et al. 2005; Ocvirk et al. 2008; Dekel et al. 2009; van de Voort et al. 2011), or used “zoom-in” simulations that do not generate strong galactic winds and hence cannot address the complex interaction between inflowing and outflowing gas in the multiphase CGM (e.g. Faucher-Giguère & Kereš 2011; Fumagalli et al. 2011; Kimm et al. 2011; Stewart et al. 2011; Goerdt et al. 2012).

In Shen et al. (2012), we presented a high-resolution analysis of the metal-enriched CGM of a massive galaxy at $z = 3$ using results from the “Eris” suite of new cosmological hydrodynamic “zoom-in” simulations, in which a close analog of a Milky Way system arises at the present epoch (Guedes et al. 2011). Such simulations adopt a blastwave scheme for supernova feedback that – in combination with a star formation recipe based on a high gas density threshold – generates galactic outflows without explicit wind particles. Shen et al. (2012) identified three sources of heavy elements within 200 physical kpc from the galaxy’s center: the main host, its satellite progenitors (accreted by the main host before redshift 3), and nearby dwarfs. The CGM was shown to be a blend of outflowing metal-rich and infalling metal-poor gas, with approximately half of all gas-phase metals locked in a hot-warm component. In this Paper we use a new simulation of the “Eris” suite to create synthetic far-UV absorption spectra through the CGM and compare them to high-redshift observations, and to make predictions about the properties and detectability of cold accretion flows. To anticipate the results of our study, the simulated transmission spectra are found to be in good agreement with the interstellar metal absorption line strengths and H I covering factors as a function of impact parameter recently measured in a $z = 2-3$ galaxy sample by Steidel et al. (2010) and Rudie et al. (2012). We show that cold accretion streams within $1-2 R_{\text{vir}}$ are traced by optically thick, metal-enriched absorbers with covering factor of 10-20%. There is no substantial suppression of the cold accretion mode caused by galactic outflows. The central galaxy is surrounded by a large halo of collisionally-ionized O VI plasma that matches the properties of the O VI bubbles recently detected around low-redshift star-forming galaxies by Tumlinson et al. (2011).

2. SIMULATION

The Eris suite of zoom-in simulations of a Milky Way galaxy analog is being performed in a *Wilkinson Microwave Anisotropy Probe* 3-year cosmology with the parallel TreeSPH code GASOLINE (Wadsley et al. 2004). Details of main run were given in Guedes et al. (2011). The high-resolution region, 1 Mpc on a side at $z = 0$, contains 13 million dark matter particles and an equal number of gas particles, for a final dark and gas particle mass of $m_{\text{DM}} = 9.8 \times 10^4 M_{\odot}$ and $m_{\text{SPH}} = 2 \times 10^4 M_{\odot}$, respectively. The spline softening length is 120 pc. The twin run analyzed here (“Eris2”) presents several improvements over the previously published versions (Guedes et al. 2011; Shen et al. 2012): 1) the initial stellar mass function (IMF) follows the modern determination by Kroupa (2001). This increases the number of Type II supernovae per unit stellar mass by about a factor of 2, and the IMF-averaged metal yield by a factor of 3 compared to Kroupa et al. (1993); 2) the metallicity-dependent radiative cooling at all temperatures in the range $100-10^9$ K is determined using pre-computed tabulated rates from the photoionization code CLOUDY (Ferland et al. 1998), following Shen et al. (2010). CLOUDY tables assume that metals are in ionization equilibrium. The ionization, cooling, and heating rates for primordial species (H, H $^+$, He, He $^+$, He $^{++}$) are calculated time-dependently from the rate equations. A uniform, cosmic UV background modifies the ionization and excitation state of the gas, photoionizing away abundant metal ions and reducing the cooling efficiency. It is implemented using the new Haardt & Madau (2012) redshift-dependent spectra, including emission from quasars and star-forming galaxies. A non-uniform local stellar radiation field is added in post-processing, as detailed below. As in previous runs, the gas is assumed to be optically thin to ionizing radiation at all wavelengths; 3) star formation occurs stochastically when cold ($T < 10^4$ K), virialized gas reaches a threshold density of $n_{\text{SF}} = 20 \text{ atoms cm}^{-3}$ (4 times higher than used in the original Eris run), and proceeds at a rate $d\rho_*/dt = 0.1\rho_{\text{gas}}/t_{\text{dyn}}$, where ρ_* and ρ_{gas} are the stellar and gas densities, and t_{dyn} is the local dynamical time; 4) star particles inject energy, mass, and metals back into the ISM through Type Ia and Type II SNe and stellar winds. We track the formation of Oxygen and Iron separately, and convert Oxygen to alpha-elements and Iron to iron-peak elements assuming solar abundances patterns (Asplund et al. 2009). In the absence of some implementation of diffusion, metals are locked into specific particles and their distribution is artificially inhomogeneous (Wiersma et al. 2009). Eris2 includes a scheme for turbulent mixing in shearing flows that redistributes heavy elements and thermal energy between wind material and the ambient gas. Following Shen et al. (2010), the mixing of any scalar quantity A is approximated by a diffusion term

$$\left(\frac{dA}{dt}\right)_D = \nabla(D\nabla A), \quad (1)$$

where the diffusion coefficient D follows the model proposed by Smagorinsky (1963) for the atmospheric boundary layer,

$$D = C |S_{ij}| h^2. \quad (2)$$

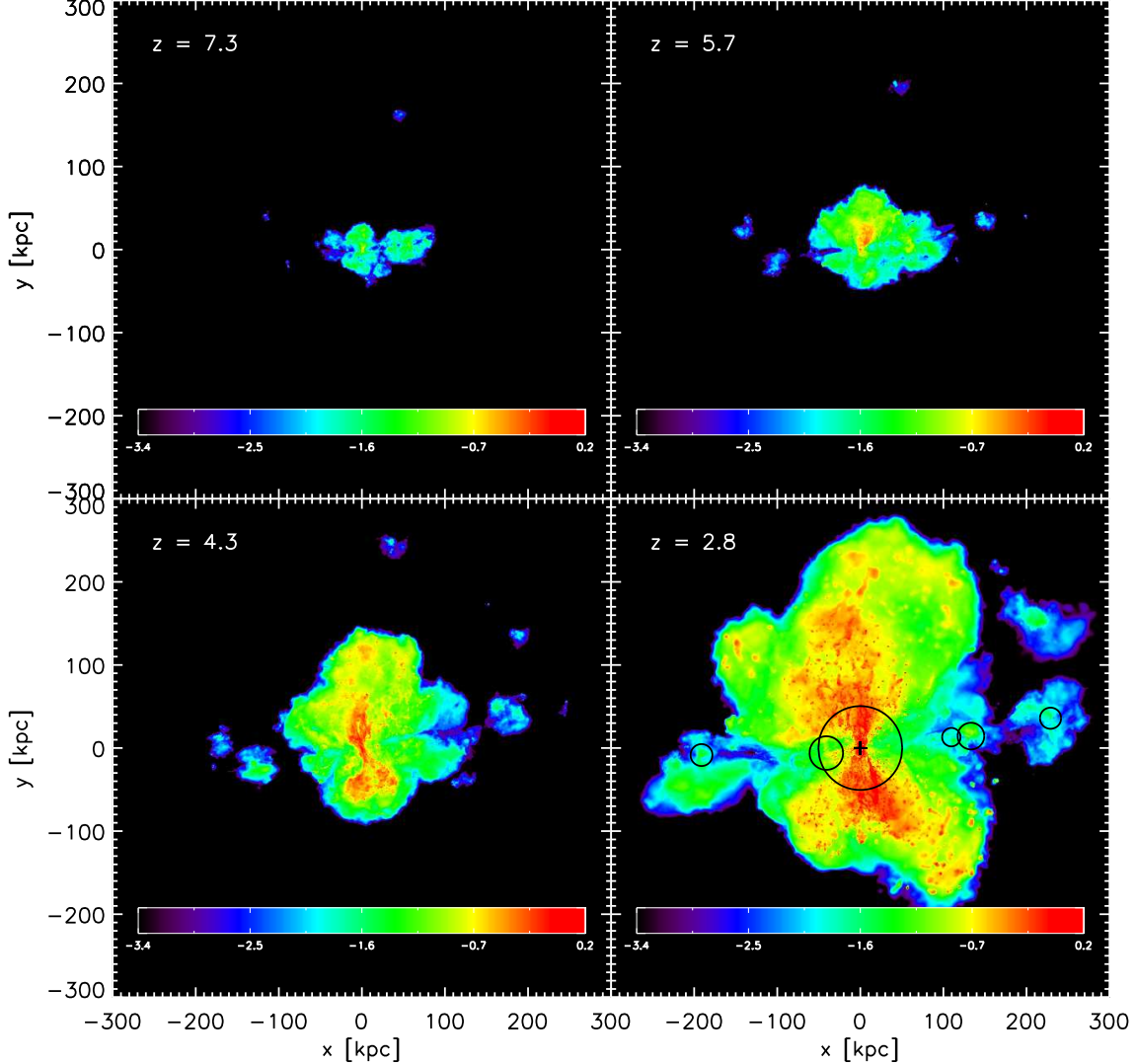


FIG. 1.— The growth of Eris2’s metal enriched CGM. The figure shows the projected gas metallicity (i.e. the surface mass density of metals divided by the total mass surface density) at different redshifts in a cube of 600 (proper) kpc on a side. The galaxy stellar disk is seen nearly edge-on in this projection. At $z = 2.8$, the galaxy center is indicated by the plus sign at coordinates $(x, y) = (0, 0)$, and its virial radius is marked by the black circle. Also marked are the virial radii of the 5 most massive nearby dwarfs and satellites. The metallicity is given in units of solar, $Z_{\odot} = 0.0142$ (Asplund et al. 2009).

Here S_{ij} is the trace-free velocity shear tensor and h is the measurement scale (taken to be equal to h_{SPH}). This choice for S_{ij} results in no diffusion for compressive or purely rotating flows. As in Shen et al. (2010), we choose a coefficient value of $C = 0.05$ expected from turbulence theory. This diffusion is applied to both thermal energy and heavy elements. Metal mixing was not implemented in the Eris and ErisMC simulations of Guedes et al. (2011) and Shen et al. (2012). The impact of metal diffusion is to spread heavy elements from out-flowing wind material to the surroundings so that more gas gets contaminated at low levels (Shen et al. 2010).

As in previous simulations of this series, the feed-

back scheme follows the recipes of Stinson et al. (2006). Each Type II SN deposits metals and a net energy of 0.8×10^{51} ergs into a ‘blastwave radius’, and the heated gas has its cooling shut off (to model the effect of feedback at unresolved scales) until the end of the momentum-conserving phase of the blastwave, which is set by the local gas density and temperature and by the total amount of energy injected (McKee & Ostriker 1977). No kinetic energy is explicitly assigned to particles within the radius of the blastwave. The energy injected by many SNe adds up to create larger hot bubbles and longer shutoff times. The main difference of this feedback model compared to other “sub-grid” schemes

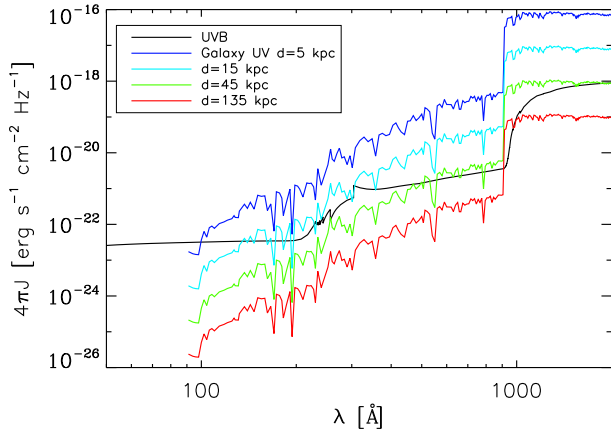


FIG. 2.— The far-UV flux impinging on Eris2’s CGM. The solid line shows the $z = 2.8$ UV diffuse background from Haardt & Madau (2012), while the colored lines show the local stellar radiation at different distances from the center, assuming an escape fraction of $f_{\text{esc}} = 3\%$ for the ionizing photons that leak from the star-forming regions into the CGM. The synthetic galaxy spectrum was produced running STARBURST99 (Leitherer et al. 1999) assuming a (constant) star formation rate of $20 \text{ M}_{\odot} \text{ yr}^{-1}$ and a Kroupa (2001) IMF.

(e.g. Springel & Hernquist 2003) is that it keeps galactic outflows hydrodynamically coupled to the energy injection by SNe. In combination with a high gas density threshold for star formation (which enables energy deposition by SNe within small volumes), this scheme has been found to be key in producing realistic dwarf galaxies (Governato et al. 2010) and late-type massive spirals (Guedes et al. 2011). We stress that the parameters of the simulation have not been finely tuned to provide a fit to any of the observations discussed in this Paper. The modifications implemented in Eris2 compared to previously published runs of this series have been simply dictated by improving and updating the physics of galaxy formation and the CGM.

2.1. Local radiation field

Aside from the isotropic cosmological UV background, Eris2’s CGM is photoionized by a local non-uniform stellar radiation field. We have run STARBURST99 (Leitherer et al. 1999) and produced a synthetic galaxy stellar spectrum assuming star formation proceeds continuously at a constant rate of $20 \text{ M}_{\odot} \text{ yr}^{-1}$ and a Kroupa (2001) IMF. The galaxy spectrum, multiplied by the distance dilution factor $(4\pi d^2)^{-1}$ (for $d > 0.9 \text{ kpc}$, where d is the distance from the center of Eris2) and by the frequency-independent (absorption cross-section weighted) fraction of ionizing photons that leaks from the star-forming regions into the CGM and IGM, $\langle f_{\text{esc}} \rangle$, has been added to the UV background to create a non-uniform radiation field. This approximation places all the stellar sources within the inner kpc, and breaks down for distances comparable to the scale length of the stellar disk. We have assumed an escape fraction of $f_{\text{esc}} = 3\%$ (close to the recent upper limit, 5% , for $z \approx 3$ LBGs derived by Boutsia et al. 2011) and run the photoionization code CLOUDY to calculate again, *in post-processing*, ionization fractions for an optically thin slab of gas at the density, temperature, metallicity, and impinging ra-

diation field of the simulated SPH particles, under the assumption that the temperature of the gas is not modified by the local radiation field.

3. ANALYSIS AND PROPERTIES OF THE CGM

At $z = 2.8$ (the lowest redshift reached by our simulation), Eris2 has a virial mass of $M_{\text{vir}} = 2.6 \times 10^{11} \text{ M}_{\odot}$, a virial radius of $R_{\text{vir}} = 50 \text{ kpc}$, a stellar mass of $M_{*} = 1.5 \times 10^{10} \text{ M}_{\odot}$ (a factor 1.4 smaller than in ErisMC, see Shen et al. 2012) and is forming stars at a rate of $\text{SFR} = 20 \text{ M}_{\odot} \text{ yr}^{-1}$. The mass loading factor at R_{vir} (characterizing the amount of material involved in the galactic outflow), $\eta = \dot{M}_w / \text{SFR}$ where \dot{M}_w is the rate at which mass is ejected, ranges from 0.2 to 0.9 in the redshift interval 2.8-3.2. Observations of galactic outflows powered by starbursts suggest a wide range of mass loading factors, $\eta = 0.01 - 10$, with no obvious correlation with the star formation rates of their hosts (Veilleux et al. 2005). While in low-resolution cosmological simulations, the mass loading factor is one of the input parameters (e.g., Oppenheimer & Davé 2008), in our SN-driven blastwave feedback scheme there is no specific parameter for mass loading.

Eris2’s baryon fraction is 0.13, and the mean gas and stellar metallicities within R_{vir} are $\langle Z_g \rangle = 0.7 Z_{\odot}$ and $\langle Z_{*} \rangle = Z_{\odot}$, respectively. The galaxy’s H II regions (defined by all gas at $T = 10^4 \text{ K}$ within 10 kpc from the center) are characterized by $12 + \log(\text{O}/\text{H}) = 8.5$, in agreement with the value, $12 + \log(\text{O}/\text{H}) = 8.42 \pm 0.06$, measured by Erb et al. (2006a) in star-forming galaxies of the same stellar mass at $\langle z \rangle = 2.2$. About half of all the gas-phase heavy elements reside in Eris2’s CGM (defined as all gas at $R > 0.2 R_{\text{vir}} = 10 \text{ kpc}$), and about half of all the CGM metals are locked in a warm-hot component at $T > 10^5 \text{ K}$. The total mass of processed material with $Z > 10^{-3} Z_{\odot}$ within 150 kpc is $4.7 \times 10^{10} \text{ M}_{\odot}$, while the mass of more pristine, $Z < 10^{-3} Z_{\odot}$, gas within the same region is $1.04 \times 10^{10} \text{ M}_{\odot}$. It is this region that will be compared in § 4 to observations of the CGM around LBGs. Figure 1 shows the projected gas-phase metallicity in a cube 500 (physical) kpc on a side at different epochs. While metal-enriched material is seen as far as 250 kpc from the center, within the same region we identify 11 dwarf satellite systems with masses above 10^9 M_{\odot} that are also forming stars and polluting the CGM of Eris2 (Shen et al. 2012; Porciani & Madau 2005). Figure 2 shows the far-UV flux impinging on Eris2’s CGM. With the adopted escape fraction, the galaxy flux at 1 Ryd dominates over the diffuse UV background at all distances $< 45 \text{ kpc}$. The most noticeable impact of the stellar radiation field will be to increase (compared to a case with $f_{\text{esc}} = 0$) the interstellar absorption line strengths of Si IV and C IV and to decrease the equivalent width of hydrogen Ly α at small impact parameters.

The processed simulation provides positions, velocities, abundances, and temperatures of the baryonic fluid elements represented by SPH particles. To study the CGM of Eris2, we draw through the simulation volume 500×500 regularly spaced sightlines within a projected distance of 250 physical kpc from the center, for three orthogonal projections of the galaxy. Each particle is spread over its 3-dimensional SPH smoothing kernel, and a line integral is taken through the smoothed distribu-

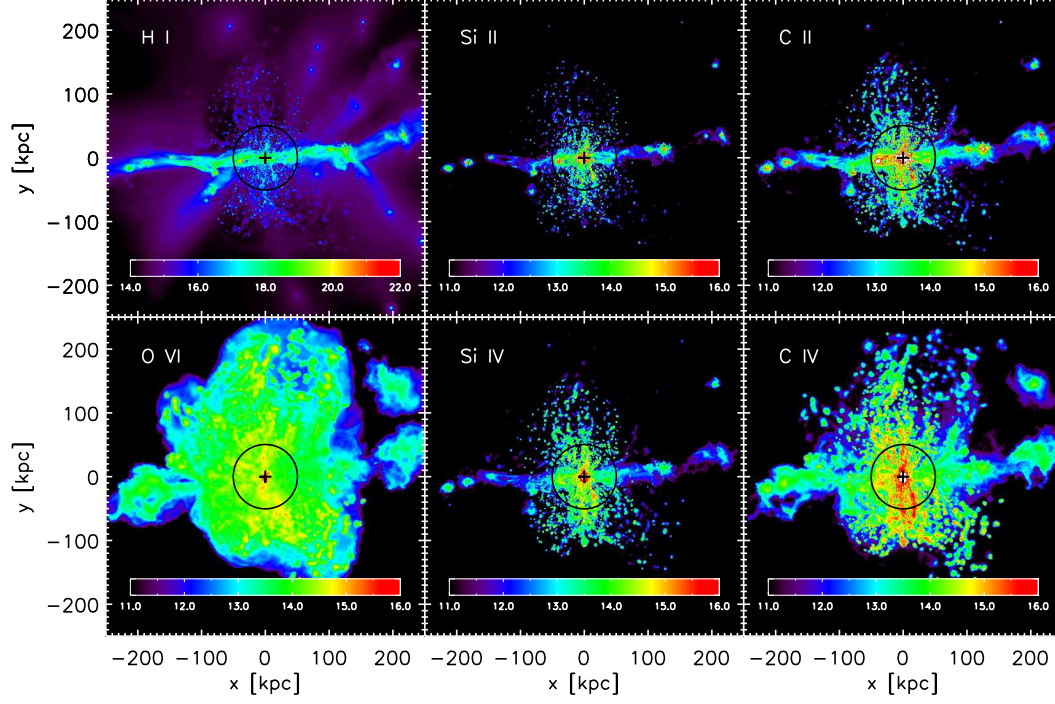


FIG. 3A.— A map of the projected column density in a cube of 500 (proper) kpc on the side from the Eris2 simulation at $z = 2.8$. The 6 panels show H I, C II, C IV, Si II, Si IV, and O VI. Intervals of column density in the range $10^{11} - 10^{22} \text{ cm}^{-2}$ for H I and $10^{11} - 10^{16} \text{ cm}^{-2}$ for all metal ions are marked in the panels with different colors.

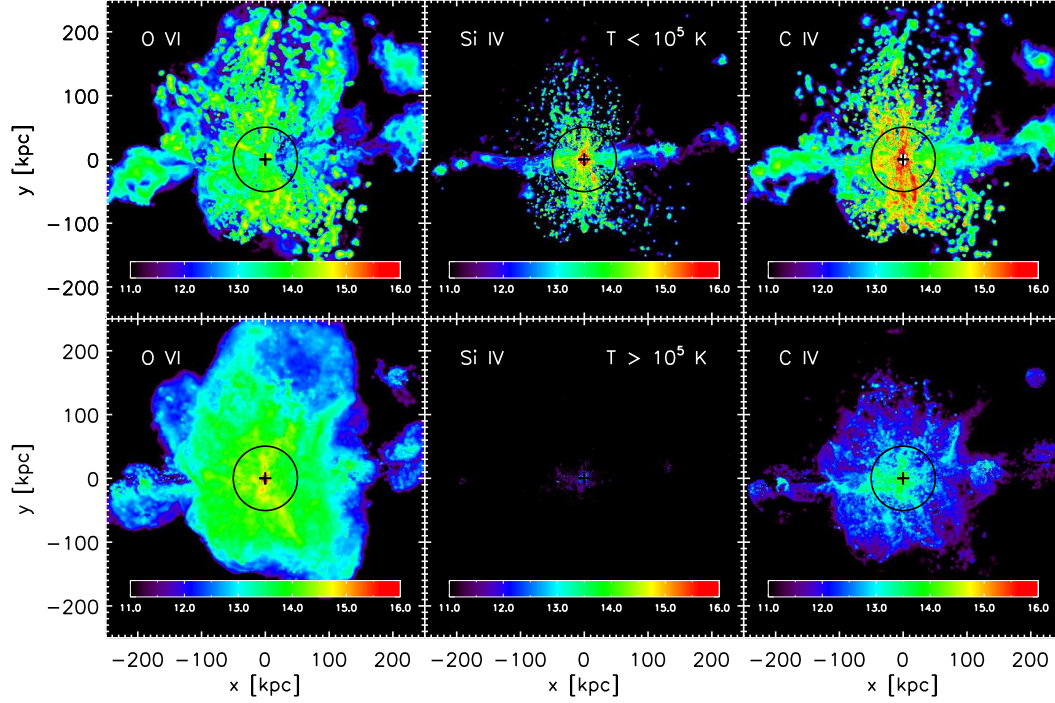


FIG. 3B.— The multi-phase nature of Eris2's CGM. Same as Fig. 3a but for cool ($T < 10^5 \text{ K}$, *top panel*) and warm-hot ($T > 10^5 \text{ K}$, *bottom panel*) gas only, as traced by the high-ionization species C IV, Si IV, and O VI.

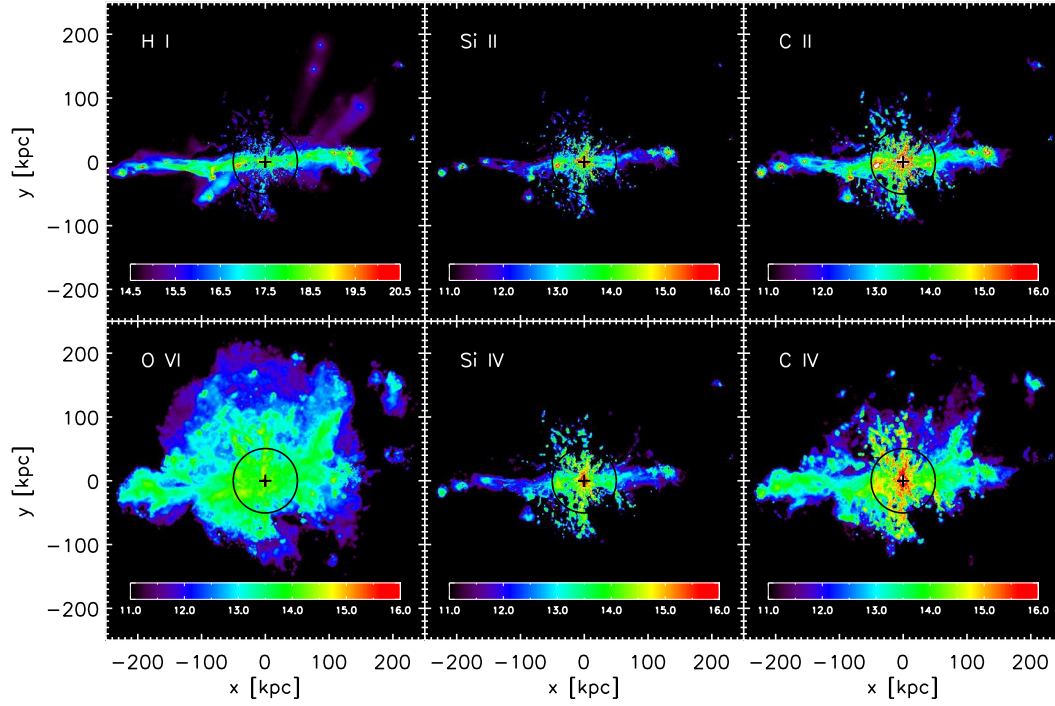


FIG. 4A.— The kinematics of Eris2's CGM. Same as Fig. 3a but for inflowing gas only, as traced by low- and high-ionization species.

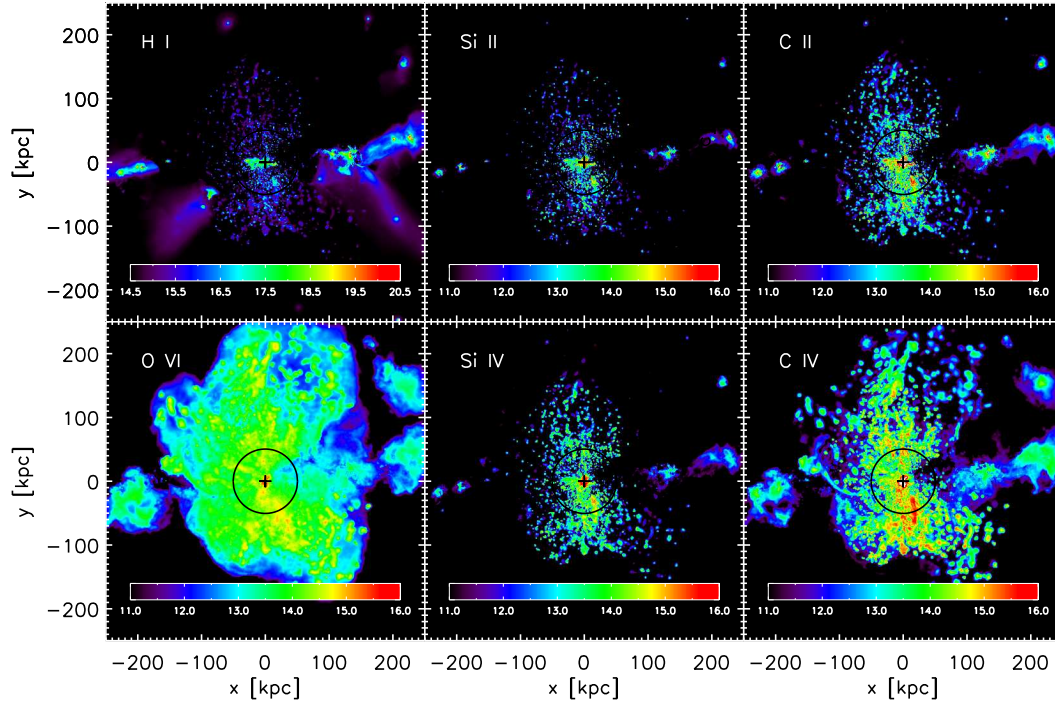


FIG. 4B.— Same as Fig. 4a but for outflowing gas only.

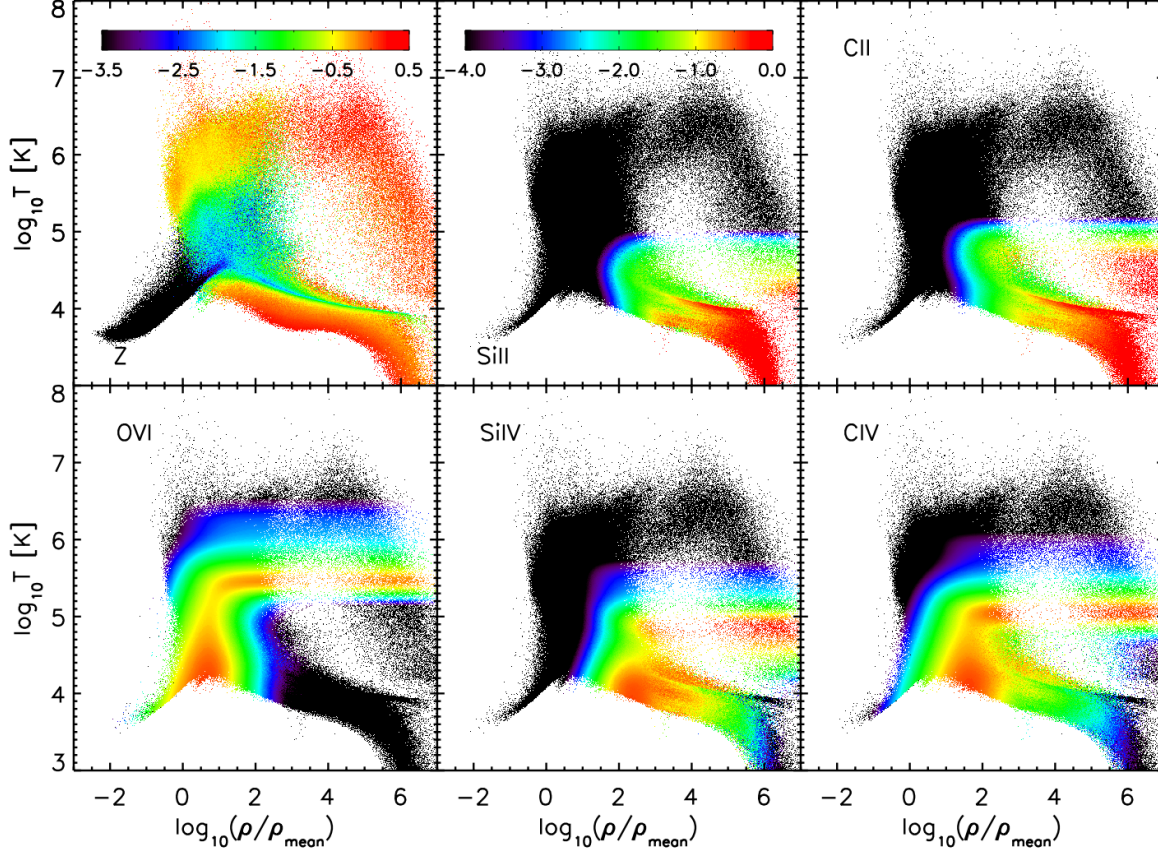


FIG. 5.— Distribution of all enriched gas in the temperature-density plane at $z = 2.8$ within the simulation volume. The top left panel shows the mass-weighted total metallicity (in units of solar), while in all the other panels the color coding indicates the ion fractions for the species C II, C IV, Si II, Si IV, and O VI. The mean baryon density of the universe at this redshift is $1.4 \times 10^{-5} \text{ cm}^{-3}$. Hot enriched gas vented out in the halo by the cumulative effect of SN explosions can be seen cooling (first adiabatically then radiatively) and raining back onto the disk in a “galactic fountain”.

tion to determine the line absorption optical depth as a function of frequency. For definiteness, the gas-phase column density, N , of an absorbing ion along a sightline of length L , is calculated as

$$\begin{aligned} N &= \sum_j \int_0^L (m_j Z_j / m) W(r_{jl}, h_j) dl \\ &= \sum_j (m_j Z_j / m) W_{2D}(r_{jl}, h_j), \end{aligned} \quad (3)$$

where m_j is the gas particle mass, Z_j its mass fraction in the relevant ion, and m is the atomic mass of the ion. This amounts to a line integral through the 3D smoothing kernel $W(r_{jl}, h_j)$ of each particle whose smoothing volume $V_j = (4/3)\pi h_j^3$ is pierced by the sightline at impact parameter r_{jl} . In the equation above we indicate with W_{2D} the 2D smoothing kernel (with units of length $^{-2}$).

Because of the assumed spline smoothing (Monaghan 1992), only SPH particles at impact parameter $r_{jl} < 2h_j$ contribute to the line integral in equation (3). Each such particle is characterized by a velocity v_j along the sightline, and by a temperature T_j , so that the total optical depth at the observed frequency ν in a given line transi-

tion can be written as

$$\tau(\nu) = \sum_j (m_j Z_j / m) W_{2D}(r_{jl}, h_j) \sigma_j(\nu), \quad (4)$$

and the integrated absorption equivalent width of the line is

$$W_0 = \frac{c}{\nu_0^2} \int [1 - e^{-\tau(\nu)}] d\nu. \quad (5)$$

Here, the absorption cross-section is expressed in terms of the Voigt function as follows:

$$\sigma_j(\nu) = \frac{s a_j}{\pi^{3/2} \Delta \nu_j} \int_{-\infty}^{+\infty} dy \frac{\exp(-y^2)}{(x_j - y)^2 + a_j^2}, \quad (6)$$

where s is the frequency integrated absorption cross-section (proportional to the oscillator strength f of the transition), $\Delta \nu_j \equiv \nu_0(b_j/c)$ is the Doppler width, $a_j \equiv \Gamma/(4\pi\Delta \nu_j)$, $x_j \equiv (\nu - \nu_j)/(\Delta \nu_j)$, $\nu_j \equiv \nu_0(1 - v_j/c)$ is the line center frequency corrected for the gas velocity along the line of sight, $b_j \equiv \sqrt{2kT_j/m}$ is the Doppler parameter, and all other symbols have their usual meaning. We assume that the galaxy is at zero velocity, and include the contribution of bulk motion and Hubble expansion to the particle velocity v_j . The flux decrement in equation (5) is integrated over $\pm 500 \text{ km s}^{-1}$ centered on the

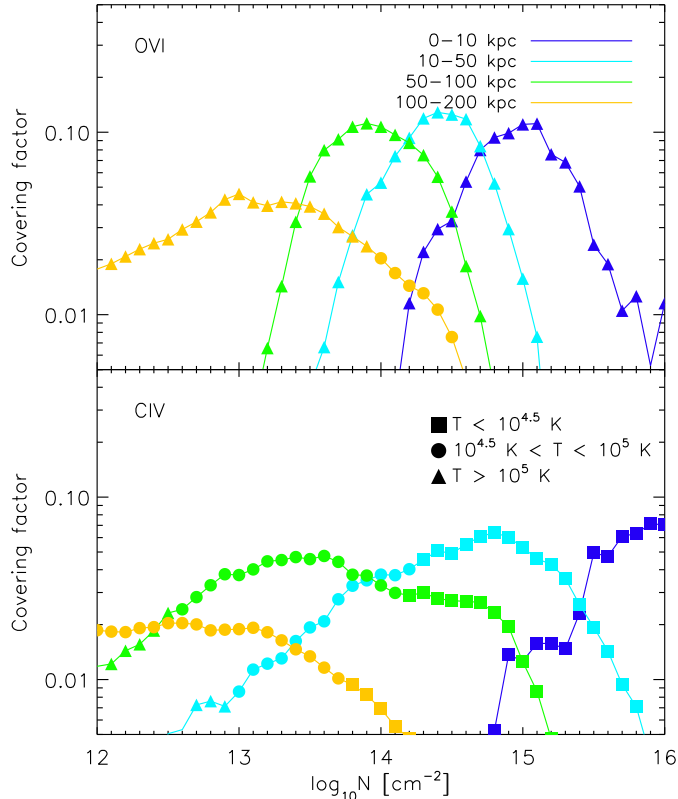


FIG. 6.— The covering factor (defined as the percentage of lines of sight with a given column density of absorbing gas, as seen by the observer) of O VI (top) and C IV (bottom) absorbing material through Eris2’s CGM as a function of column density N . Values are plotted in bins of $\Delta \log N = 0.1$. The color coding marks covering factor in different ranges of impact parameter, 0–10 kpc (dark blue), 10–50 kpc (cyan), 50–100 kpc (green), 100–200 kpc (yellow). Different symbols are used to indicate the median temperature of a given column of absorbing gas over all sightlines: $T < 10^{4.5}$ K (squares), $10^{4.5} < T < 10^5$ K (circles), and $T > 10^5$ K (triangles).

galaxy’s position, and each line of sight passes through a simulation volume 1 Mpc (physical) across.

Figures 3a and 3b show the total projected column densities in H I, C II, C IV, Si II, Si IV, and O VI for Eris2’s $z = 2.8$ CGM, and the columns of high ionization species that are cool and warm-hot, respectively. Figures 4a and 4b show the same columns for inflowing and outflowing CGM material only (gas particles are separated in inflowing and outflowing according to the sign of their radial velocities relative to the center of the main host), while the distribution of all enriched gas in the temperature-density plane is depicted in Figure 5.

Metal-enriched outflows are bipolar and perpendicular to the plane of the disk. Heavy elements are clearly spread over a large range of phases, from cold star-forming material at $T < 10^4$ K and $n \gtrsim n_{\text{SF}} = 20$ atoms cm^{-3} (corresponding to $\delta \equiv \rho/\rho_{\text{mean}} \gtrsim 10^{6.15}$ at $z = 2.8$) to hot $T > 10^6$ K low density $\delta \simeq 1$ intergalactic gas that cannot cool radiatively over a Hubble time. O VI is diffuse, has a large covering factor, and extends beyond $4R_{\text{vir}} = 200$ kpc from the center of Eris2. C IV absorption is much clumpier and less extended than O VI, while

low-ionization species like C II and Si II trace narrow inflowing streams as well as dense outflowing clumps. The covering fraction of low-ionization species declines faster than that of O VI or C IV.

Inflows and outflows coexist in Eris2, with about one third of all the gas within R_{vir} found to be outflowing. At R_{vir} , the mean metallicity of inflowing gas is $0.05 Z_{\odot}$, while the mean metallicity of outflowing gas is $0.56 Z_{\odot}$ (the average is taken over all gas particles within a thin shell of radius R_{vir} and thickness $0.02 R_{\text{vir}}$). Inflowing enriched gas traces large-scale cold filaments that penetrate deep into the virial radius (see Fig. 4a and § 4.2), as well as material raining back onto the disk as part of a “galactic fountain”. About 77%, 32%, 44%, 66%, 50%, and 66% of the total H I, O VI, C IV, C II, Si IV, and Si II mass within $2R_{\text{vir}}$, respectively, is inflowing. High H I column density absorption mainly traces the narrow cold inflowing streams. Outflowing material has smaller H I columns and contributes to the covering factor of gas with $N_{\text{HI}} > 10^{15.5} \text{ cm}^{-2}$.

The distribution of high-ionization species in the temperature-density plane is clearly bimodal. At high densities and temperatures, ions are in collisional ionization equilibrium (CIE) and their fractional abundances are only a function of temperature. At lower densities, when photoionization is dominant, the equilibrium abundances become a function of density as well as temperature, and metals are typically in a higher ionization state at a given temperature than in CIE. C II and Si II ions trace primarily cool, $10^4 \lesssim T \lesssim 10^5$ K photoionized CGM gas at overdensities $\log \delta \simeq 2$ (as well as dense, cold disk neutral material), which extends as far as $2R_{\text{vir}}$ but with a covering factor that decreases sharply beyond R_{vir} (Fig. 3a). Si IV and C IV are abundant in low density $\log \delta \gtrsim 1$ photoionized gas. C IV ions maintain a significant covering factor beyond $2R_{\text{vir}}$ and can also be detected in warm-hot and denser $\log \delta \sim 2$ CGM gas within R_{vir} .

Within 100 kpc, O VI is largely collisionally ionized and traces CGM gas with $\log \delta \gtrsim 1$ and $T > 10^5$ K (in collisional ionization equilibrium, O VI reaches its peak abundance fraction, ~ 0.2 , at 3×10^5 K). A cool, $T \lesssim 5 \times 10^4$ K clumpy O VI component with smaller covering factor becomes dominant at large galactocentric distances. This is relatively high column, moderate overdensity $\log \delta \sim 0.5 - 1.5$ gas that was enriched and expelled by nearby dwarfs and is photoionized by the cosmic UV background. The mass ratios of the hot versus cold O VI populations are 17:1, 1.6:1, and 0.7:1 at distances $d < R_{\text{vir}}$, $R_{\text{vir}} < d < 2R_{\text{vir}}$, and $2R_{\text{vir}} < d < 3R_{\text{vir}}$, respectively.

The covering factor of O VI and C IV absorbing material through Eris2’s CGM is plotted in Figure 6 as a function of column density. The color coding marks the covering factor in different ranges of galactocentric impact parameter, while different symbols are used to indicate the median temperature of a given column of absorbing gas over all sightlines. The figure shows how C IV absorbers with large covering factors are typically cool (photoionized), while the opposite is true for O VI. A hot C IV component is also present at small impact parameters and low columns.

The formalism developed in this Section can be finally

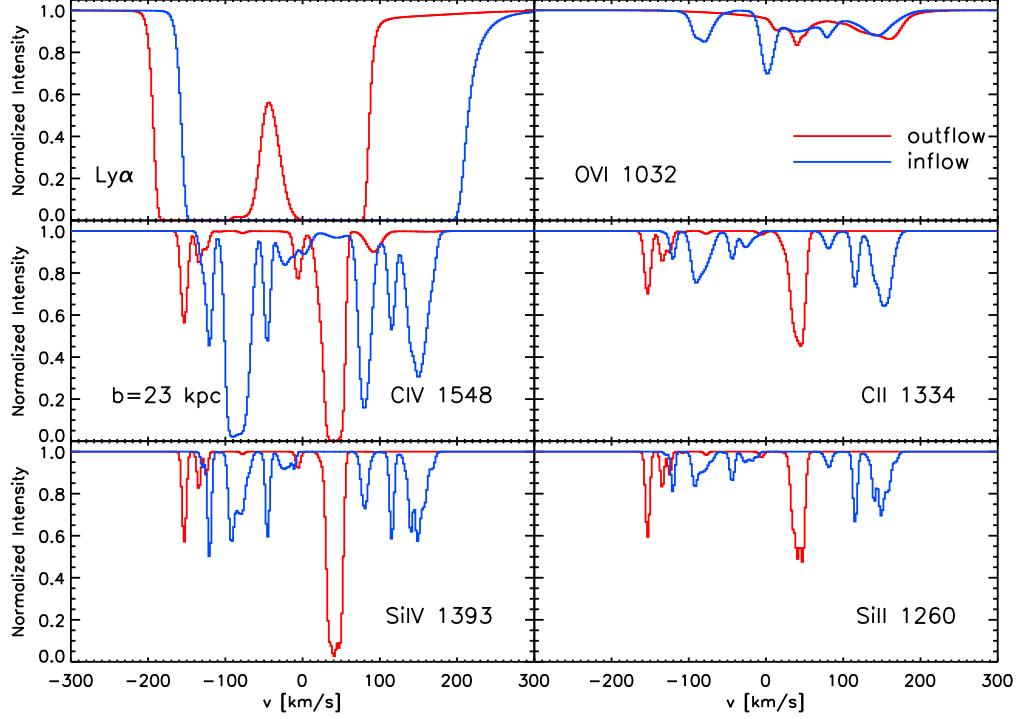


FIG. 7A.— A simulated absorption spectrum through Eris2's CGM at $z = 2.8$, computed at a resolution of 2 km s^{-1} and plotted in velocity space. A random sightline at impact parameters $b = 0.46 R_{\text{vir}} = 23 \text{ kpc}$ from the galaxy center is shown. Gas with positive radial velocity with respect to systemic is redshifted. The total column densities of the absorbing H I, C II, C IV, Si II, Si IV, and O VI ions are, respectively 2.6×10^{16} , 1.1×10^{14} , 4.2×10^{14} , 8.7×10^{12} , 5.3×10^{13} , and $1.3 \times 10^{14} \text{ cm}^{-2}$.

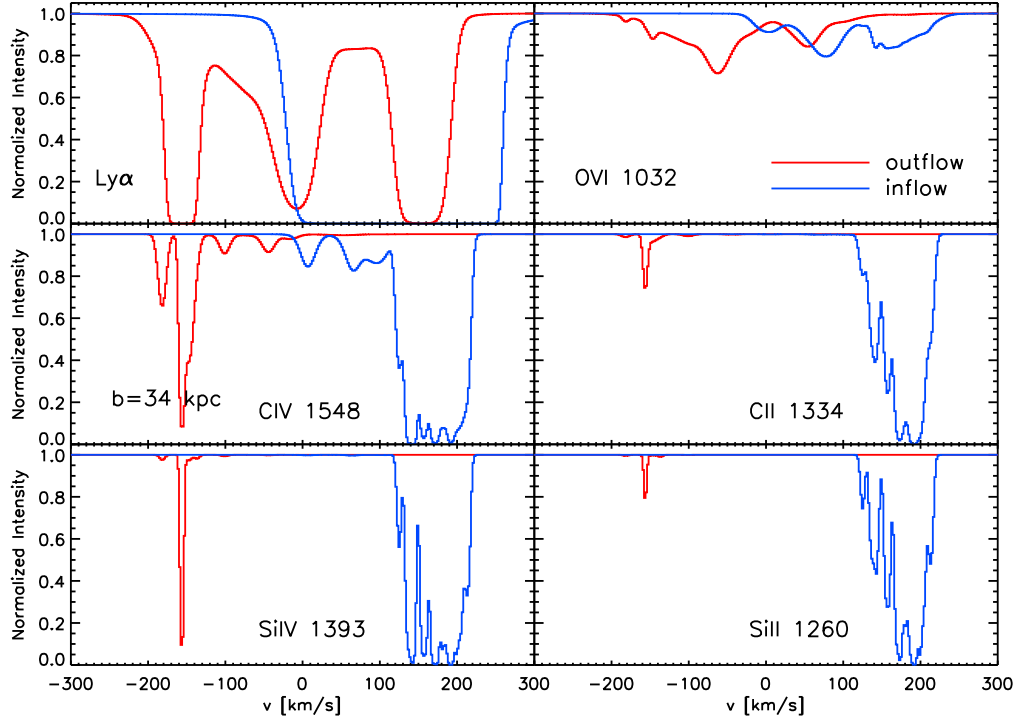


FIG. 7B.— Same as Fig. 7a, but for a sightline at impact parameter $b = 34 \text{ kpc}$. The total column densities of the absorbing H I, C II, C IV, Si II, Si IV, and O VI ions are, respectively 1.3×10^{17} , 4.2×10^{14} , 4.6×10^{14} , 3.7×10^{13} , 1.3×10^{14} , and $1.8 \times 10^{14} \text{ cm}^{-2}$.

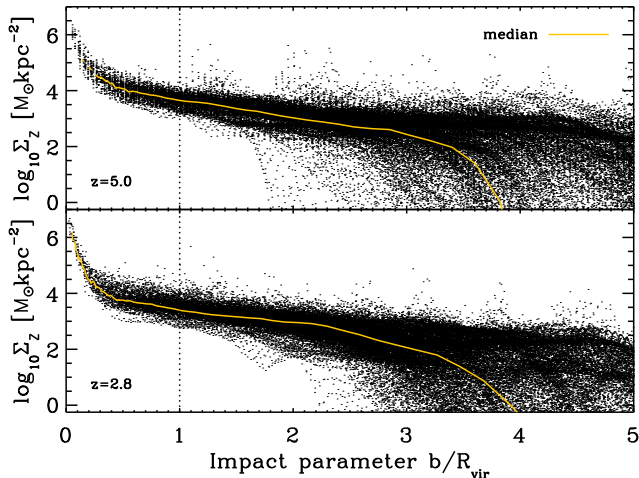


FIG. 8.— Total projected metal mass density, Σ_Z , along each sightline through Eris2’s CGM, as a function of galactocentric impact parameter, b , in units of the virial radius. The metal mass density is plotted at two different redshifts, $z = 2.8$ ($R_{\text{vir}} = 50$ kpc) and $z = 5$ ($R_{\text{vir}} = 19$ kpc). The density of black points (one for each sightline) is a measurement of the covering factor of heavy elements in the simulation. The solid yellow line shows the median value of Σ_Z at a given b/R_{vir} . At the two redshifts, the metal bubbles around Eris2 appear scaled versions of each other.

used to compute the optical depth of the hydrogen Ly α $\lambda 1216$, C II $\lambda 1334$, C IV $\lambda\lambda 1548, 1550$, Si II $\lambda 1260$, Si IV $\lambda 1393$ and O VI $\lambda 1032$ transitions. Figures 7a and 7b show artificial absorption spectra along two lines of sight through the CGM at impact parameters $b = 23$ kpc and $b = 34$ kpc from Eris2’s center, plotted on a galactocentric velocity scale. Column densities range from $8.7 \times 10^{12} \text{ cm}^{-2}$ for Si II to $1.3 \times 10^{17} \text{ cm}^{-2}$ for hydrogen Ly α , and individual components span a radial velocity range from about -200 to $+200 \text{ km s}^{-1}$. Velocity profiles are complex, with outflowing and inflowing gas detected at positive (redshifted) and negative (blueshifted) projected velocities from the near and the far side of the galaxy. The simultaneous presence, in velocity space, of features from singly ionized species as C II and Si II along with higher-ionization species reflects the multiphase structure of the simulated CGM. The sightline depicted in Figure 7b goes through cool, metal-enriched gas infalling on the near side of the galaxy. The inflowing component is distributed in physical space between R_{vir} and $2R_{\text{vir}}$, has overdensities $\log \delta \gtrsim 2$, metallicities in excess of $0.03 Z_{\odot}$, and is part of the metal-enriched zone around a dwarf satellite companion accreting along a filament. We will discuss the observability of cold accretion streams via low-ionization metal lines in the next section. The spectrum shows several outflowing components, including solar-metallicity photoionized gas at $v \sim -150 \text{ km s}^{-1}$ that is being ejected by the main host, as well as pristine IGM gas at $v \sim 0 \text{ km s}^{-1}$ that is located $\gtrsim 240$ kpc from the galaxy center.

A detailed analysis of interstellar absorption line strengths as a function of redshift will be the subject of another paper. Here, it is important to keep in mind that, when properly scaled, the property of Eris2 CGM are not changing rapidly with cosmic time. Figure 8 shows the total projected metal mass density, Σ_Z , along

each sightline, as a function of galactocentric impact parameter in units of the virial radius, b/R_{vir} . The metal mass density is plotted at two different redshifts, $z = 2.8$ ($R_{\text{vir}} = 50$ kpc) and $z = 5$ ($R_{\text{vir}} = 19$ kpc). The density of black points (one for each sightline) is a measurement of the covering factor of metal-enriched material in the simulation. At the two redshifts, the metal bubbles around Eris2 appear scaled versions of each other.

4. COMPARISON WITH THE OBSERVATIONS

4.1. Circumgalactic metals at $z=2-3$

The close pair sample of galaxies at $\langle z \rangle = 2.2$ of Steidel et al. (2010), drawn from a spectroscopic survey of “BX” UV-color selected objects, provides a robust map of cool circumgalactic gas at galactocentric impact parameters $b = 3 - 125$ kpc. Objects in this sample have been well-characterized in terms of their spatial clustering and stellar population parameters (Adelberger et al. 2005a; Erb et al. 2006b). A good match to both the observed clustering strength and the space density of the “BX” galaxies to dark matter halos in the Millennium simulation is obtained for an average halo mass of $\langle M_{\text{vir}} \rangle = 9 \times 10^{11} M_{\odot}$ (Conroy et al. 2008). The virial radius for a halo at the average mass that formed several 10^8 yr prior to the epoch of observation is $R_{\text{vir}} = 80$ kpc (Steidel et al. 2010), close to the scale at which low-ionization absorption lines become weaker. This suggests that beyond R_{vir} absorbers may become too diffuse and highly ionized to produce significant columns of low-ionization metals (Steidel et al. 2010). With a virial mass at $z = 2.8$ of $M_{\text{vir}} = 2.6 \times 10^{11} M_{\odot}$ and a radius $R_{\text{vir}} = 50$ kpc, Eris2 is a smaller counterpart to Steidel et al. (2010) close pair sample galaxies.⁶ For a proper comparison between simulation data and observations, we have therefore scaled the impact parameter with the virial radius of the mean halo in the pair sample (80 kpc) and with the Eris2’s virial radius in the simulation, and plotted the observed and predicted line strengths against the correspondingly normalized impact parameters. Along every simulated sightline, the rest-frame equivalent widths W_0 of C II 1334, C IV 1549 (including both components of the doublet), Si II 1260, and Si IV 1393 are shown in Figure 9 versus b/R_{vir} , together with the values observed in the composite spectra of foreground galaxies (placed at $\langle b \rangle = 1$ kpc) and background galaxies (at $\langle b \rangle = 31, 63, 103$ kpc) by Steidel et al. (2010). The density of black points is a measurement of the covering factor of absorbing material at a given impact parameter in the simulation. We plot W_0 along every artificial line of sight rather than an average over all sightlines in order to underline the dispersion in the measured line strengths as well as the contribution of satellite galaxies (the narrow “spikes” in equivalent width seen at $b/R_{\text{vir}} > 1$). For each species, the strength of absorption declines rapidly around $b = 1-2 R_{\text{vir}}$. The agreement between the simulation and the observations is rather good: except perhaps for a slight deficit in the covering factor of C II and Si II around $\sim 0.8 R_{\text{vir}}$ and an excess of C IV at large impact parameters, Eris2’s simulated CGM broadly reproduces the line strengths-impact parameter

⁶ This is also true in the luminous component, as the mean stellar mass of the spectroscopic sample, $\langle M_{\star} \rangle = (3.6 \pm 0.4) \times 10^{10} M_{\odot}$ (Erb et al. 2006b), is 2.5 times larger than in Eris2.

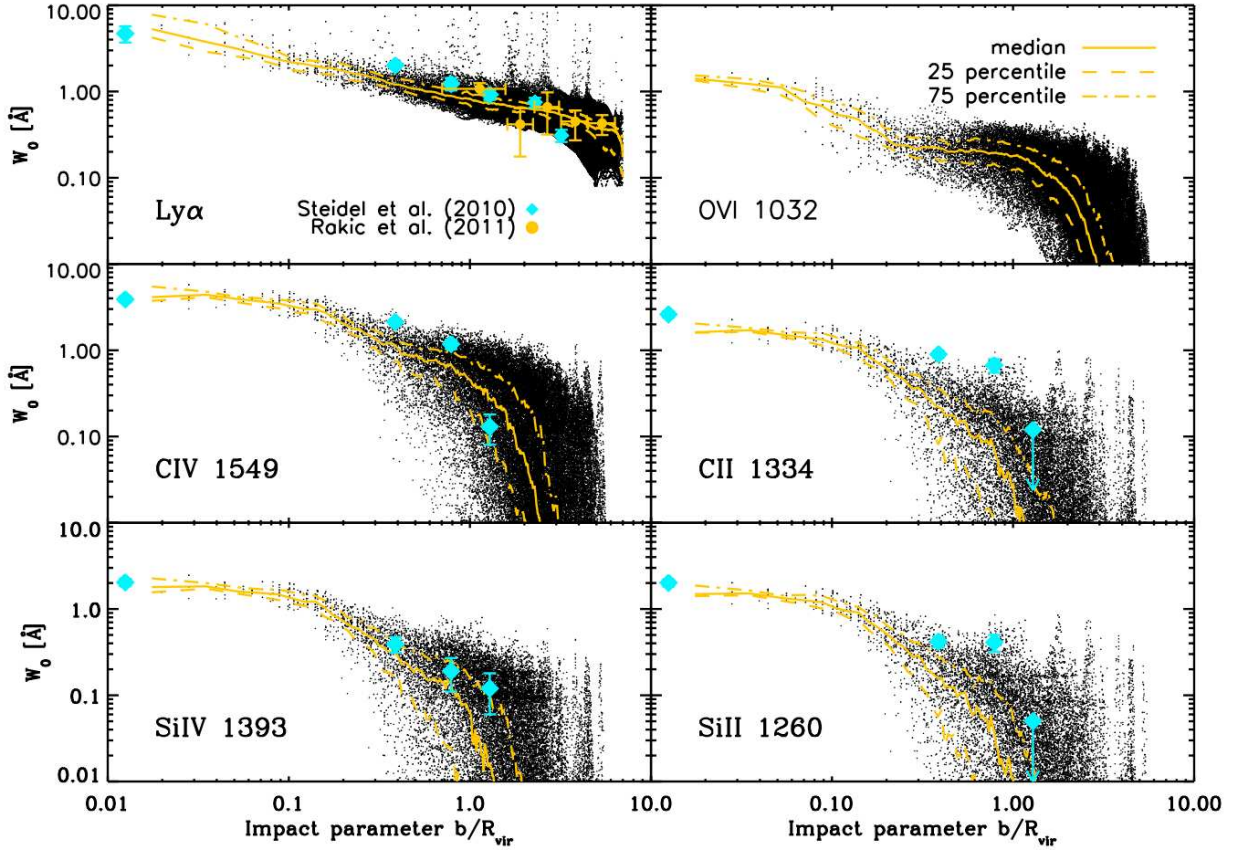


FIG. 9.— Interstellar absorption line strengths of the 1216 Ly α , 1334 C II, 1549 C IV, 1260 Si II, 1393 Si IV, and 1032 O VI transitions as a function of galactocentric impact parameter b in physical kpc. Values for C IV include both components of the $\lambda\lambda 1548, 1550$ doublet. The cyan points at $b=1, 31, 63$, and 103 kpc are data from Steidel et al. (2010), with downward arrows on points indicating upper limits. The yellow points in the top left panel are data from Rakic et al. (2012). The impact parameter has been normalized to $R_{\text{vir}} = 80$ kpc (see text for details). The black dots show the rest-frame equivalent widths measured along artificial sightlines through the CGM of our Eris2 simulation at $z = 2.8$, and the yellow lines marks the median and the 25th and 75th percentiles.

trends observed by Steidel et al. (2010). In particular, the covering factor of absorbing material declines less rapidly with impact parameter for Ly α and C IV (and O VI) compared to C II, Si IV, and Si II, with Ly α remaining strong ($W_{\text{Ly}\alpha} > 300 \text{ m}\text{\AA}$) to $\gtrsim 5R_{\text{vir}} = 250$ kpc. At small impact parameters, where lines are mostly saturated, the equivalent width along a sightline is modulated by the velocity structure of the absorbing material. The kinematics of Eris2’s inner CGM appears therefore to be consistent with the observations. A comparison between Figure 9 and Figure 15 of Fumagalli et al. (2011) shows that the predicted interstellar Si II equivalent widths are about an order of magnitude larger in Eris2 than in Fumagalli et al. (2011), and therefore that strong galactic outflows are an essential ingredient for a quantitative modeling of the CGM.

4.2. Circumgalactic H I and cold flows

Figure 9 also shows the equivalent width of hydrogen Ly α absorption as a function of impact parameter for the galaxy-galaxy pair sample of Steidel et al. (2010)

as well as the QSO-galaxy pair sample of Rakic et al. (2012). Again, the simulation agrees well with the observations, as Ly α remains strong ($W_{\text{Ly}\alpha} > 300 \text{ m}\text{\AA}$) to $5R_{\text{vir}} = 250$ kpc. Infall of cool gas via narrow streams, directly onto the central regions of galaxies, is the mode of gas accretion that is predicted to feed star formation in high redshift galaxies like Eris2 (e.g. Kereš et al. 2005; Dekel & Birnboim 2006; Ocvirk et al. 2008; Agertz, Teyssier, & Moore 2009; Dekel et al. 2009). Observational signatures of cold accretion streams at high redshift are key for testing our understanding of the flows of matter, energy, and metals into and out of galaxies. Absorption by neutral hydrogen (and, as we shall argue below, by low-ionization metal lines) is a promising way to observe the cold streams. Recent observations of $2.0 \lesssim z \lesssim 2.8$ star-forming galaxies near a QSO sightline (the Keck Baryonic Structure Survey) show that the covering fraction of absorbers of various N_{HI} columns around galaxies ranges from $90 \pm 9\%$ ($< R_{\text{vir}}$) to $68 \pm 9\%$ ($< 2R_{\text{vir}}$) for $\log N_{\text{HI}} > 15.5$, and from $30 \pm 14\%$ ($< R_{\text{vir}}$) to $28 \pm 9\%$ ($< 2R_{\text{vir}}$) for Lyman

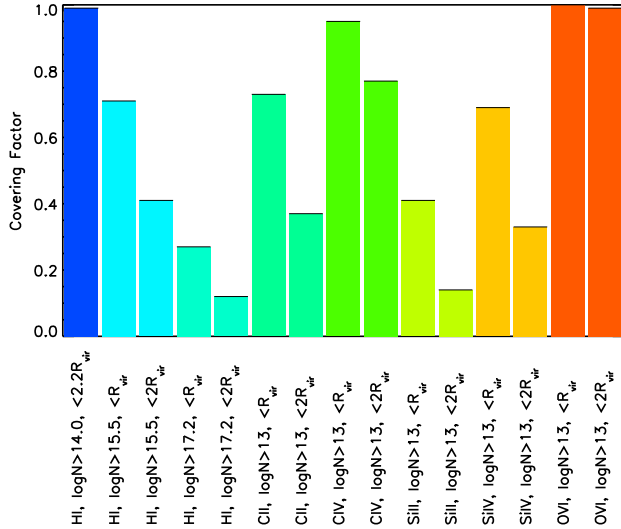


FIG. 10.— The covering factor at different galactocentric impact parameters of absorbers of various species and column densities (in cm^{-2}) in Eris2’s CGM.

Limit Systems (LLSs) with $\log N_{\text{HI}} > 17.2$ (Rudie et al. 2012).

The simulation (see Fig. 10) yields covering factors of 71% and 27% ($< R_{\text{vir}}$) and of 41% and 12% ($< 2R_{\text{vir}}$) for $\log N_{\text{HI}} > 15.5$ and > 17.2 , again in reasonable agreement with the data, albeit perhaps on the low side for the largest impact parameters. According to Rudie et al. (2012), the incidence of absorbers with $\log N_{\text{HI}} > 14.5$ is found to be higher near galaxies than in the general IGM. The covering factor of $\log N_{\text{HI}} > 14$ systems within $2.5 R_{\text{vir}}$ is observed to be $92 \pm 5\%$ vs. 99% in Eris2. Eris2’s covering factor of LLSs appears comparable or higher than those predicted at high redshift by Faucher-Giguère & Kereš (2011) and Fumagalli et al. (2011) for galaxies in the same mass range. Both these groups ran high-resolution cosmological hydrodynamical simulations that do not generate strong galactic outflows (Fumagalli et al. 2011 using the AMR technique, Faucher-Giguère & Kereš 2011 using SPH as in Eris2), combined with radiative transfer. Because our hydrodynamical simulations lack proper ionizing radiative transfer, we cannot correctly address the covering factor of the self-shielded, thicker Damped Ly α (DLA) absorbers with $\log N_{\text{HI}} \gtrsim 20.3$.

It is interesting at this stage to look at the properties of cold streams. About 90% of all optically thick absorbing gas within 1-2 virial radii is found to be inflowing with radial velocities $\lesssim 150 - 200 \text{ km s}^{-1}$. Figures 11a and 11b shows two projections of all *inflowing* material with $\log N_{\text{HI}} > 17.2$, as traced by H I and C II, respectively. The streams can be clearly seen penetrating deep inside the virial radius and delivering cold gas to the central galaxy. Enriched to metallicities above 0.01 solar by previous episodes of star formation in the main host and nearby dwarfs (Shen et al. 2012; Fumagalli et al. 2011), the streams give origin to strong ($N_{\text{CII}} > 10^{13} \text{ cm}^{-2}$) C II absorption with a covering factor of 22% within R_{vir} and 10% within $2R_{\text{vir}}$, which should make the presence of cold flows detectable with metal absorption lines.

We find no substantial suppression of the cold accretion mode caused by galactic-scale mass outflows. The mass inflow rate of cold ($T < 10^5 \text{ K}$) gas into Eris2 is $\dot{M}_{\text{cold}} = 18 \text{ M}_{\odot} \text{ yr}^{-1}$ (measured at R_{vir}), in agreement with the results of Kereš et al. (2009) for galaxies in the same redshift and mass range as Eris2, and comparable to Eris2’s star formation rate. About 35% of the cold gas mass is brought in by dwarf satellite galaxies. The cold mode dominates over the hot mode, which is characterized by an accretion rate of $\dot{M}_{\text{hot}} = 5 \text{ M}_{\odot} \text{ yr}^{-1}$. The distribution of metallicity, column density weighted, in the entire sample of inflowing LLSs within $2R_{\text{vir}}$ is centered around a median value of $0.07 Z_{\odot}$, significantly higher than found in the simulations of Fumagalli et al. (2011); Kimm et al. (2011). Nearly all inflowing LLSs have metallicities above 0.01 solar (Figure 12).

4.3. The O VI halos of star-forming galaxies

As already discussed in the previous section, as a consequence of the SN blastwave-driven galactic outflows generated in our simulations, the central galaxy is surrounded by a large halo of collisionally ionized O VI. Ubiquitous, large (150 kpc) halos of O VI around low-redshift star-forming galaxies have been recently detected in a survey with the Cosmic Origins Spectrograph onboard of the *HST* (Tumlinson et al. 2011), and it is interesting to compare their properties with our simulation. The Tumlinson et al. (2011) sample includes galaxies with stellar masses $9.5 < \log (M_{*}/\text{M}_{\odot}) < 11.2$ and specific star formation rates $-11 < \log (\text{sSFR}/\text{yr}^{-1}) < -9$. Eris2’s stellar mass and sSFR at $z = 2.8$ are in the middle and on the high side of such ranges, respectively. We have computed the total O VI column along simulated sightlines at different impact parameters and plotted the results in Figure 13 together with the Tumlinson et al. (2011) and Prochaska et al. (2011) low-redshift observations. Our high-redshift simulated galaxy again matches the trends observed in similar systems at low redshifts, with typical column densities of $N_{\text{OVI}} \gtrsim 10^{14} \text{ cm}^{-2}$ and a near unity covering factor are maintained all the way out to 100-150 kpc.

5. SUMMARY

Recent observations of the CGM of star-forming galaxies at high and low redshift have called for more stringent comparisons with hydrodynamical simulations of galaxy formation. The high-resolution “zoom-in” simulation presented here, Eris2, adopts a blastwave scheme for supernova feedback which, in combination with a high gas density threshold for star formation, has been shown to generate large-scale galactic outflows and be key in producing realistic dwarf galaxies and late-type massive spirals (e.g. Governato et al. 2010; Guedes et al. 2011), in turning dark matter cusps into cores (e.g. Pontzen & Governato 2012), and in enriching the CGM of high redshift LBGs (Shen et al. 2012). Simulations of star-forming galaxies run to $z = 0$ have recently stressed the importance of strong stellar feedback in reproducing the O VI hot gaseous halos observed in local galaxies (Stinson et al. 2011). Eris2 includes metal-dependent radiative cooling, a model for the diffusion of metals and thermal energy, and a local UV radiation field added in

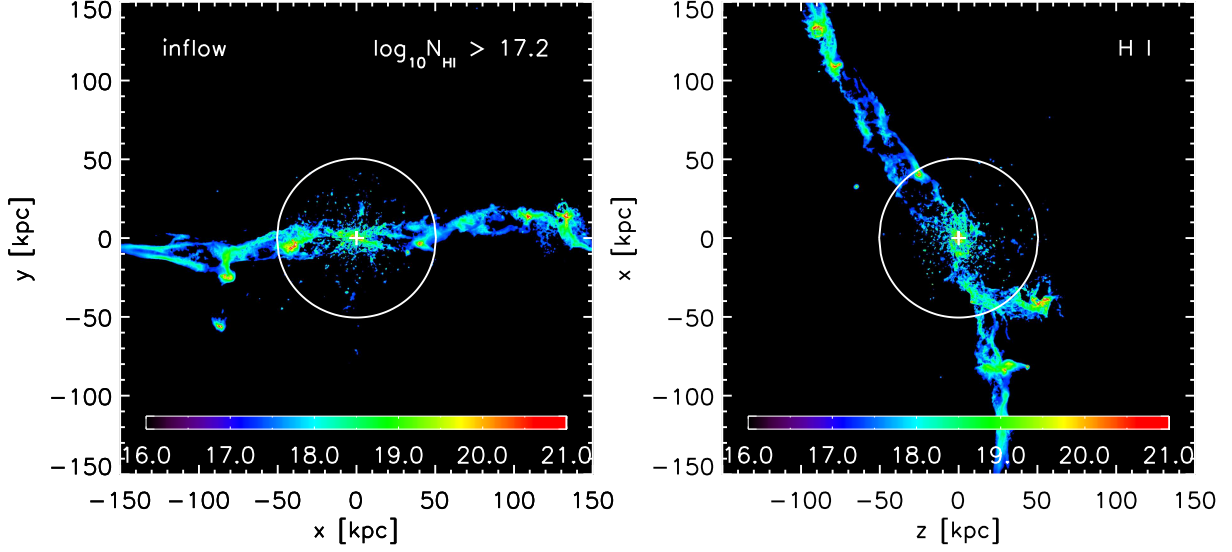


FIG. 11A.— Cold accretion streams in Eris2: a map of hydrogen column density showing inflowing, optically thick material with $\log N_{\text{HI}} > 17.2$ for 2 different projections. Eris2’s virial radius is marked by the white circle.

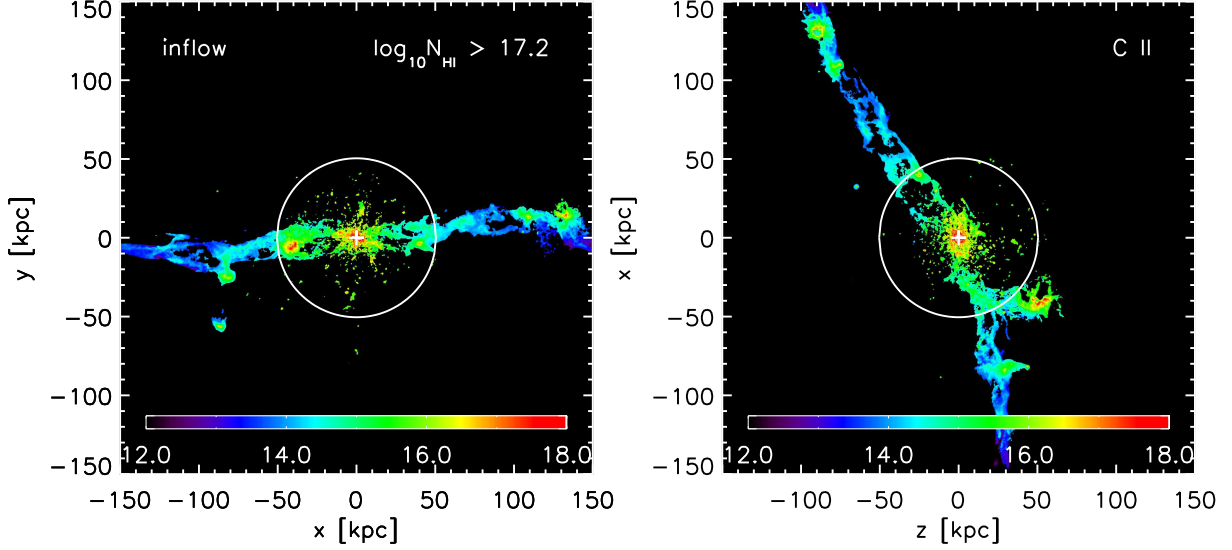


FIG. 11B.— Same as Fig. 11a, showing the C II column for optically thick inflowing gas.

post-processing, and is ideally suited for a detailed study of the kinematics, thermal and ionization state, and spatial distribution of metal-enriched gas in the CGM of massive galaxies at redshift ~ 3 . The results presented in this paper do not depend sensitively on metal diffusion: a twin simulation without diffusion produces a slightly clumpier CGM, but the impact on the covering factor of metal ions is small.

We have generated synthetic spectra by drawing sight-lines through the simulated CGM at different galactocentric impact parameters, and compared the theoretical in-

terstellar absorption line strengths with the observations. We emphasize again that the parameters of the simulation have not been tuned to provide a fit to observations of the CGM. In our examination we have found that:

- Eris2’s CGM at $z = 2.8$ contains multiple phases having a wide range of physical conditions, with half of all gas-phase metals locked in a warm-hot component at $T > 10^5$ K. Outflows and inflows co-exist, and about one third of all the gas within R_{vir} is outflowing. Inflows bring in material along optically thick “cold” streams. The streams are en-

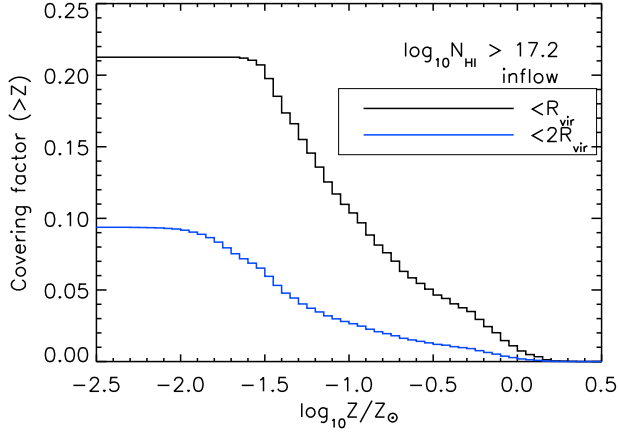


FIG. 12.— Cold, optically thick streams in Eris2 are metal-enriched. The cumulative covering factor of $\log N_{\text{HI}} > 17.2$ inflowing material above a metallicity Z is plotted within R_{vir} and $2R_{\text{vir}}$. Streams within R_{vir} ($2R_{\text{vir}}$) are enriched above 0.03 (0.01) solar by previous episodes of star formation in the main host and in dwarf satellite galaxies.

riched to metallicities above 0.01 solar by previous episodes of star formation in the main host and in nearby dwarfs.

- The C II and Si II ions trace primarily cool, $10^4 < T < 10^5$ K photoionized CGM gas at overdensities $\log \delta \simeq 2$ extending as far as $2R_{\text{vir}}$, but with a covering factor that decreases sharply beyond R_{vir} . The distributions of high-ionization species are clearly bimodal, with ions in CIE at high densities and temperatures, and with photoionization becoming dominant at low densities. C IV ions maintain a significant covering factor beyond $2R_{\text{vir}}$ and can also be detected in warm-hot and denser $\log \delta \sim 2$ CGM gas within R_{vir} . The O VI diffuse halo extends beyond $4R_{\text{vir}} = 200$ kpc from the center. Within 100 kpc, O VI is largely collisionally ionized and traces CGM gas with $\log \delta \gtrsim 1$ and $T > 10^5$ K. A cool, clumpy O VI component, photoionized by the cosmic UV background, becomes increasingly important at larger distances.
- Synthetic spectra generated by drawing sightlines through the simulated CGM produce interstellar absorption line strengths of Ly α , C II, C IV, Si II, and Si IV as a function of galactocentric impact parameter (scaled to the virial radius) that are in good agreement with those observed at high-redshift by Steidel et al. (2010) (and Rakic et al. 2012 in the case of Ly α). The covering factor of absorbing material is found to decline less rapidly with impact parameter for Ly α and C IV (and O VI) compared to C II, Si IV, and Si II. Ly α remains strong to $\gtrsim 5R_{\text{vir}} = 250$ kpc. At small impact parameters, where lines are mostly saturated, the equivalent width along a sightline is modulated by the velocity structure of the absorbing material. The kinematics of Eris2's inner CGM appears therefore to be consistent with the observations. Note that, contrary to the spherically outflowing

wind model of Steidel et al. (2010), in our simulations inflowing material contributes significantly to the absorption in the $W_0 - b$ plane.

- At small impact parameters, the local galactic UV flux increases the abundance of high-ionization species like C IV and Si IV, and decreases that of C II, Si II, and H I. O VI is largely collisionally ionized within 100 kpc, so the effect of the local UV on O VI is small. More quantitatively, within R_{vir} , galactic radiation increases the total amount of O VI by 1%, C IV by 128%, and Si IV by 146%, while it decreases C II by 53%, Si II by 51%, and H I by 87%. Nevertheless, the effect on the equivalent widths of Ly α and metal transitions is small. This is because absorption lines are saturated in the local CGM and their equivalent widths are mainly determined by the kinematics and covering factor of the gas rather than by its column density.
- The fraction of sightlines within one virial radius that intercept optically thick, $N_{\text{HI}} > 10^{17.2} \text{ cm}^{-2}$ gas is 27%, in good agreement with recent observations by Rudie et al. (2012) who find $30 \pm 14\%$. Within $2R_{\text{vir}}$, our covering factor is 12%, below the $28 \pm 9\%$ observed by Rudie et al. (2012). The corresponding covering factors for $\log N_{\text{HI}} > 15.5$ are (71%, 41%) versus ($90 \pm 9\%$, $68 \pm 9\%$) found in the observations.
- Optically thick material is found to trace cold accretion streams that penetrate deep inside the virial radius and deliver cold gas to the central galaxy. The streams have metallicities above 0.01 solar. C II absorption with $N_{\text{CII}} > 10^{13} \text{ cm}^{-2}$ arises from such streams with a covering factor of 22% and 10% within one and two virial radii, respectively, making the presence of cold flows detectable with metal absorption lines. There is no substantial suppression of the cold accretion mode caused by galactic outflows.
- The O VI halo gives origin to CGM absorption with a typical column density of $N_{\text{OVI}} \gtrsim 10^{14} \text{ cm}^{-2}$ and a near unity covering factor that is maintained all the way out to 150 kpc. This matches the trends recently observed in star-forming galaxies at low redshift by Tumlinson et al. (2011) and Prochaska et al. (2011).

While our zoom-in simulations of this single system appear then to reproduce quantitatively the complex baryonic processes that determine the exchange of matter, energy, and metals between galaxies and their surroundings, we acknowledge a number of caveats to the work presented here. Radiation transport is not explicitly present in our simulations, and while we have checked the robustness of our conclusion with a self-shielding approximation used in post-processing, simulations that incorporate some form of radiative transfer are in the making. Eris2's interstellar absorption features do not reach the maximum velocities $|v_{\text{max}}| \simeq 800 \text{ km s}^{-1}$ observed in LBGs by Steidel et al. (2010), and zoom-in simulations of more massive systems are needed in order to fully test our galactic outflow model against observations of the

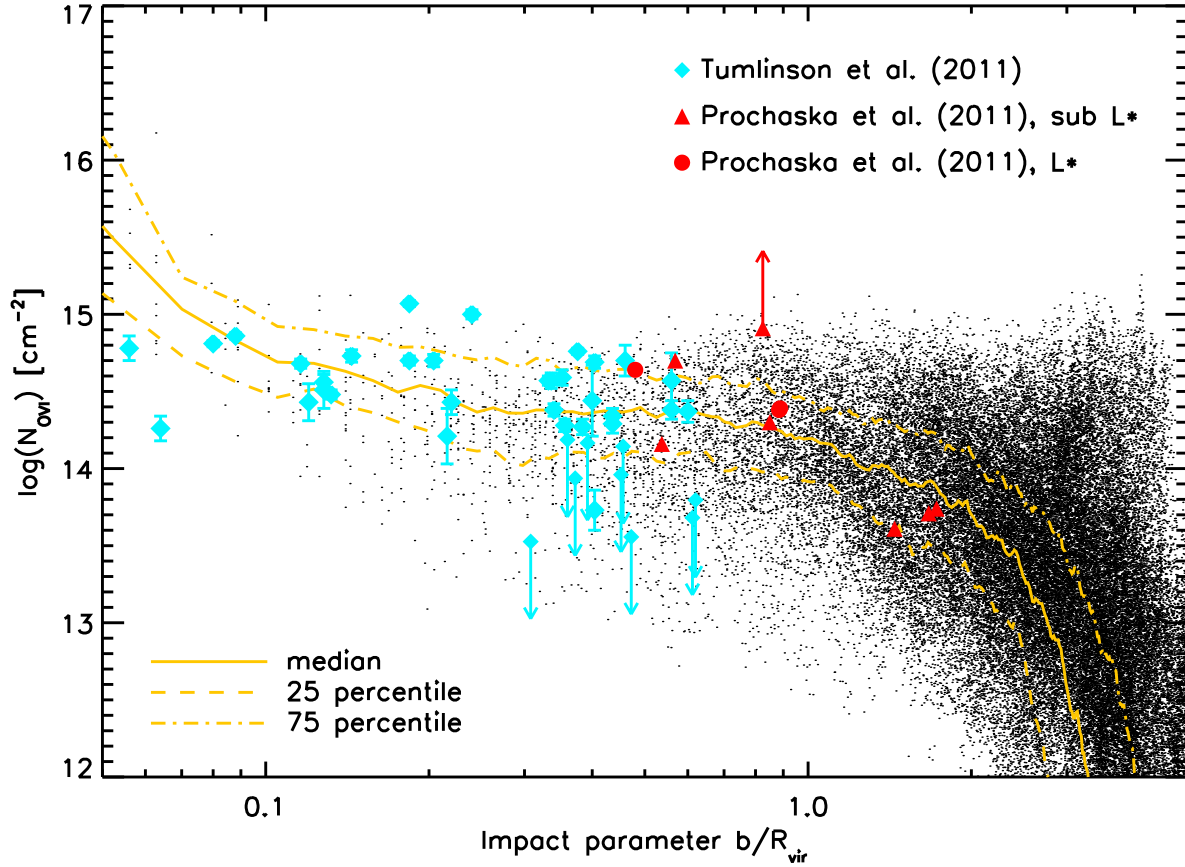


FIG. 13.— The O VI column density vs. impact parameter for the star-forming subsample of Tumlinson et al. (2011) (*cyan squares*) and the L_* (*red dots*) and sub- L_* (*red triangles*) subsamples of Prochaska et al. (2011) of low-redshift galaxies. The L_* data of Prochaska et al. (2011) and those of Tumlinson et al. (2011) have been scaled assuming a virial radius of 250 kpc. The sub- L_* data of Prochaska et al. (2011) have been scaled assuming a virial radius of 160 kpc. The black dots show the O VI column density measured along artificial sightlines through the CGM of our Eris2 simulation at $z = 2.8$, and the yellow lines marks the median and the 25th and 75th percentiles.

high-redshift CGM. The clumpiness of Eris2's CGM may, at least partly, be a numerical artifact of the SPH technique. A clumpy, two-phase medium could be produced by thermal instabilities in the warm/hot halo around the main host (Maller & Bullock 2004; Kaufmann et al. 2006, 2009), although whether or not the conditions for thermal instabilities to operate are met in real galaxies is still a controversial issue (Binney et al. 2009). The process has been observed in idealized simulations in which gas cools out of an initially uniformly hot corona and the instability is seeded by Poisson-noise density fluctuations in the initial particle distributions. Kereš & Hernquist (2009) have argued that clouds arise naturally in realistic cosmological hydrodynamical simulations as a result of a combination of Rayleigh-Taylor instabilities at the interface between cold accretion flows and the hot phase and thermal instabilities. Moreover, hot outflows and winds from supernovae launched from the disk might induce strong, large wavelength fluctuations that are not

easily damped, and may thus act as the seeds to thermal instability in the CGM. These seeding mechanisms, as well as perturbations by satellites, may all play a role in our simulations. A detailed analysis of the clumpiness of Eris2's CGM as the possible result of such instabilities will be the topic of future work.

Support for this work was provided by the NSF through grant AST-0908910 and OIA-1124453, and by NASA through grant NNX12AF87G (P.M.). Resources supporting this work were provided by the NASA High-End Computing (HEC) Program through the NASA Advanced Supercomputing (NAS) Division at Ames Research Center. J.G. was partially funded by the ETH Zurich Postdoctoral Fellowship and the Marie Curie Actions for People COFUND Program. We acknowledge useful discussions on the topics of the paper with A. Aguirre, S. Bertone, A. Dekel, M. Fumagalli, and J. Werk.

REFERENCES

- Adelberger, K. L., Steidel, C. C., Pettini, M., Shapley, A. E., Reddy, N. A., & Erb, D. K. 2005, *ApJ*, 619, 697
 Agertz, O., Teyssier, R., & Moore, B. 2009, *MNRAS*, 397, L64
 Asplund, M., Grevesse, N., Sauval, A. J., & Scott, P. 2009, *ARA&A*, 47, 481
 Binney, J., Nipoti, C., Fraternali, F. 2009, *MNRAS*, 397, 1804
 Birnboim, Y., & Dekel, A. 2003, *MNRAS*, 345, 349
 Boutsia, K. et al. 2011, *ApJ*, 736, 41
 Brooks, A. M., Governato, F., Quinn, T., Brook, C. B., & Wadsley, J. 2009, *ApJ*, 694, 396

- Cen, R., & Chisari, N. E. 2011, *ApJ*, 731, 11
- Conroy, C., Shapley, A. E., Tinker, J. L., Santos, M. R., & Lemson, G. 2008, *ApJ*, 679, 1192
- Crighton, N. H. M., et al. 2011, *MNRAS*, 414, 28
- Dekel, A., & Birnboim, Y. 2006, *MNRAS*, 368, 2
- Dekel, A., Birnboim, Y., Engel, G., Freundlich, J., Goerdt, T., Mumcuoglu, M., Neistein, E., Pichon, C., Teyssier, R., & Zinger, E. 2009, *Nature*, 457, 451
- Erb, D. K., Shapley, A. E., Pettini, M., Steidel, C. C., Reddy, N. A., & Adelberger, K. L. 2006a, *ApJ*, 644, 813
- Erb, D. K., Steidel, C. C., Shapley, A. E., Pettini, M., Reddy, N. A., Adelberger, K. L. 2006b, *ApJ*, 646, 107
- Goerdt, T., Dekel, A., Sternberg, A., Ceverino, D., Teyssier, R., & Primack, J. R. 2010, *MNRAS*, 407, 613
- Goerdt, T., Dekel, A., Sternberg, A., Gnat, O., & Ceverino, D. 2012, *MNRAS*, 424, 2292
- Governato, F., et al. 2010, *Nature*, 463, 203
- Guedes, J., Callegari, S., Madau, P., & Mayer, L. 2011, *ApJ*, 742, 76
- Faucher-Giguère, C.-A., & Kereš, D. 2011, *MNRAS*, 412, L118
- Ferland, G. J., Korista, K. T., Verner, D. A., Ferguson, J. W., Kingdon, J. B., & Verner, E. M. 1998, *PASP*, 110, 761
- Fumagalli, M., Prochaska, J. X., Kasen, D., Dekel, A., Ceverino, D., & Primack, J. R. 2011, *MNRAS*, 418, 1796
- Haardt, F., & Madau, P. 2012, *ApJ*, 746, 125
- Kacprzak, G. G., Churchill, C. W., Steidel, C. C., Spitler, L. R., & Holtzman, J. A. 2012, *MNRAS*, 427, 3029
- Kaufmann, T., Bullock, J. S., Maller, A. H., Fang, T., & Wadsley, J. 2009, *MNRAS*, 396, 191
- Kaufmann, T., Mayer, L., Wadsley, J., Stadel, J., & Moore, B. 2006, *MNRAS*, 370, 1612
- Kereš, D., Katz, N., Weinberg, D. H., & Davé, R. 2005, *MNRAS*, 263, 2
- Kereš, D., Katz, N., Fardal, M., Davé, R., & Weinberg, D. H. 2009, *MNRAS*, 395, 160
- Kereš, D., & Hernquist, L. 2009, *ApJ*, 700, L1
- Kimm, T., Slyz, A., Devriendt, J., & Pichon, C. 2011, *MNRAS*, 413, L51
- Kroupa, P. 2001, *MNRAS*, 322, 231
- Kroupa, P., Tout, C. A., & Gilmore, G. 1993, *MNRAS*, 262, 545
- Leitherer, C., Schaerer, D., Goldader, J. D., Gonzalez Delgado, R. M., Robert, C., Kune, D. F., de Mello, D. F., Devost, D., & Heckman, T. M. 1999, *ApJS*, 123, 3
- Maller, A. H., & Bullock, J. S. 2004, *MNRAS*, 355, 694
- McKee, C. F., & Ostriker, J. P. 1977, *ApJ*, 218, 148
- Monaghan, J. J. 1992, *ARA&A*, 30, 543
- Ocvirk, P., Pichon, C., & Teyssier, R. 2008, *MNRAS*, 390, 1326
- Oppenheimer, B. D., & Davé, R. 2008, *MNRAS*, 387, 577
- Pettini, M., Shapley, A. E., Steidel, C. C., Cuby, J.-G., Dickinson, M., Morwood, A. F. M., Adelberger, K. L., & Giallisco, M. 2001, *ApJ*, 569, 742
- Pontzen, A., & Governato, F. 2012, *MNRAS*, 421, 3464
- Porciani, C., & Madau, P. 2005, *ApJL*, 625, L43
- Prochaska, J. X., & Hennawi, J. F. 2009, *ApJ*, 690, 1558
- Prochaska, J. X., Weiner, B., Chen, H.-W., Mulchaey, J., & Cooksey, K. 2011, *ApJ*, 740, 91
- Rakic, O., Schaye, J., Steidel, C. C., & Rudie, G. C. 2012, *ApJ*, 751, 94
- Rudie, G. C., Steidel, C. C., Trainor, R. F., Rakic, O., Bogosavljevic, M., Pettini, M., Reddy, N., Shapley, A. E., Erb, D. K., Law, D. R. 2012, *ApJ*, 750, 67
- Shapley, A. E., Steidel, C. C., Pettini, M., & Adelberger, K. L. 2003, *ApJ*, 588, 65
- Shen, S., Wadsley, J., & Stinson, G. 2010, *MNRAS*, 407, 1581
- Shen, S., Madau, P., Aguirre, A., Guedes, J., Mayer, L., & Wadsley, J. 2012, *ApJ*, 760, 50
- Smagorinsky, J., 1963, *Monthly Weather Rev.*, 91, 3, 99
- Springel, V., & Hernquist, L. 2003, *MNRAS*, 339, 312
- Steidel, C. C., Erb, D. K., Shapley, A. E., Pettini, M., Reddy, N., Bogosavljević, M., Rudie, G. C., & Rakic, O. 2010, *ApJ*, 717, 289
- Stewart, K. R., Kaufmann, T., Bullock, J. S., Barton, E. J., Maller, A. H., Diemand, J., & Wadsley, J. 2011, *ApJ*, 735, L1
- Stinson, G. S., et al. 2012, *MNRAS*, 425, 1270
- Stinson, G., Seth, A., Katz, N., Wadsley, J., Governato, F., & Quinn, T. 2006, *MNRAS*, 373, 1074
- Tumlinson, J., et al. 2011, *Science*, 334, 948
- Veilleux, S., Cecil, G., & Bland-Hawthorn, J. 2005, *ARA&A*, 43, 769
- van de Voort, F., Schaye, J., Booth, C. M., Haas, M. R., & Dalla Vecchia, C. 2011, *MNRAS*, 414, 2458
- Wadsley, J. W., Stadel, J., & Quinn, T. 2004, *New Astronomy*, 9, 137
- Weiner, B. J., et al. 2009, *ApJ*, 692, 187
- Wiersma, R. P. C., Schaye, J., Theuns, T., Dalla Vecchia, C., & Tornatore, L. 2009, *MNRAS*, 399, 574